

# Microfluidics: Continuous-Flow Synthesis of Nanoparticle Dispersions for the Fabrication of Organic Solar Cells

Karen Fischer, Philipp Marlow, Felix Manger, Christian Sprau, and Alexander Colsmann\*

State-of-the-art solvents for the fabrication of organic solar cells are mostly toxic or hazardous. First attempts to deposit light-harvesting layers from aqueous or alcoholic nanoparticle dispersions instead have been successful on laboratory scale, enabling future eco-friendly production of organic solar cells. In this work, a scalable high-throughput continuous-flow microfluidic system is employed to synthesize surfactant-free organic semiconductor dispersions by nanoprecipitation. By adjusting the differential speed of the syringe pumps, the concentration of the initial solute and the irradiation of the microfluidic chip, the synthesis can be controlled for tailored dispersion concentrations and nanoparticle sizes. The resulting dispersions are highly reproducible, and the semiconductor inks are stable for at least one year. The synthesis of the dispersions is exemplified on a polymer/fullerene combination with large-scale availability.

## 1. Introduction

Among the emerging photovoltaic technologies, organic bulk-heterojunction (BHJ) solar cells stand out with their color variability, their freeform design, their low weight, and their optional semitransparency.<sup>[1,2]</sup> They show potential for low-cost and environmentally sustainable fabrication and an unsurpassed energy payback time between days and a few months.<sup>[3]</sup> Printing and coating processes are widely considered for large-scale processing of organic solar cells (OSCs), warranting high-throughput and providing design flexibility. The respective inks must be tailored for the specific printing processes and best thin-film quality. On lab scale, most inks are based on halogenated solvents that are often harmful to the environment, toxic or carcinogenic. Though technically feasible, deploying those inks in large-scale printing processes would require elaborated

solvent capture facilities and hence increase the production costs. Unfortunately, most light-harvesting organic semiconductors are insoluble in eco-friendly solvents such as water or alcohols. To mitigate this solubility issue, nanoparticle dispersions from light-harvesting blends of polymers and fullerenes have been investigated in recent years towards an all-sustainable solar cell production, vastly omitting toxic solvents.

Two routes to obtain nanoparticle dispersions from polymers or polymer/fullerene blends have been reported in the literature: The most often followed route is the miniemulsion method, where small droplets of polymer solution are dispersed


in a nonsolvent by ultrasonication, stabilized by surfactants.<sup>[4]</sup> Then the solvent is removed by thermal evaporation, yielding a dispersion of solid nanoparticles. Because surfactant inclusions in the light-harvesting layer can be deleterious to the performance of the solar cell, excess surfactant must be reduced by laborious dialysis after nanoparticle formation.<sup>[5]</sup> Nevertheless, once accomplished, surfactant-stabilized organic semiconductor nanoparticles can enable the fabrication of efficient solar cells.<sup>[6–8]</sup> An alternative route to the synthesis of organic nanoparticle dispersions uses nanoprecipitation. This method produces neat dispersions of organic semiconductors or semiconductor blends without any surfactants. In batch processing, a solution of the organic semiconductor is injected into a miscible nonsolvent under stirring. Due to the miscibility of solvent and nonsolvent, the solubility of the organic semiconductor blend is reduced immediately, leading to rapid nanoparticle formation. Employing poly(3-hexylthiophene-2,5-diyl) (P3HT) and the fullerene indene-C<sub>60</sub> bisadduct (ICBA), this rapid nanoprecipitation produced BHJ-type nanoparticles which then translated to organic solar cells with PCEs of 4%, which is close to the performance of solar cells fabricated from halogenated solvents.<sup>[9,10]</sup> Recently, we revealed that electrostatic repulsion of the BHJ nanoparticles promotes the stability of surfactant-free dispersions and that irradiation during nanoprecipitation can enhance the charging of nanoparticles.<sup>[11]</sup>

The transition from lab-scale to large-area coating of semiconductor inks on roll-to-roll machines calls for a scalable and reproducible synthesis of nanoparticle inks which is difficult to achieve with batch processing in beakers or industrial equivalents. The fabrication of nanoparticle dispersions in a continuous-flow system would be the method of choice for best scalability and reproducibility.

In the past, microfluidic systems were used for controlled continuous-flow syntheses in drug manufacturing, for live cell

K. Fischer, P. Marlow, F. Manger, C. Sprau, A. Colsmann  
Karlsruhe Institute of Technology (KIT)  
Material Research Center for Energy Systems  
Strasse am Forum 7, 76131 Karlsruhe, Germany  
E-mail: alexander.colsmann@kit.edu

K. Fischer, P. Marlow, F. Manger, A. Colsmann  
Karlsruhe Institute of Technology (KIT)  
Light Technology Institute  
Engesserstrasse 13, 76131 Karlsruhe, Germany

 The ORCID identification number(s) for the author(s) of this article can be found under <https://doi.org/10.1002/admt.202200297>.

© 2022 The Authors. Advanced Materials Technologies published by Wiley-VCH GmbH. This is an open access article under the terms of the Creative Commons Attribution License, which permits use, distribution and reproduction in any medium, provided the original work is properly cited.

DOI: 10.1002/admt.202200297

microscopic imaging in biomedical science as well as for chemical analysis and lab-on-a-chip applications in molecular and biological analysis – just to name a few.<sup>[12–15]</sup> They offer rapid mixing of small amounts of liquids within channels with diameters of less than 500 μm and excellent scalability.

In this work, we demonstrate the synthesis of organic BHJ nanoparticles for the fabrication of OSCs using a micromixer chip embedded in a microfluidic system. Besides the principal scalability of microfluidic systems, this nanoprecipitation process is well controllable, and the reproducibility of the nanoparticle size is improved over the common batch nanoprecipitation approach.

## 2. Results and Discussion

### 2.1. Choice of Organic Semiconductors

For the principal investigation of the nanoparticle synthesis in a microfluidic system, we have deliberately chosen the “fruit-fly” of organic photovoltaics, P3HT, in combination with the acceptor ICBA. Although more efficient light-harvesting semiconductors are known today, this choice enables best comparison with the literature where the same material combination is regularly used to investigate the fabrication of OSCs from nanoparticle dispersions. Not least, high-throughput processes demand substantial amounts of semiconductors with constant quality and little batch-to-batch variations, which is best warranted by the synthesis of large P3HT batches. Chloroform was used as solvent for the P3HT:ICBA (1:1 w/w) blend, while ethanol was implemented as miscible nonsolvent. Notably, at this process stage, the use of chloroform does not conflict with the goal of eco-friendly processing, as the chloroform can be extracted and captured in a controlled chemistry environment after nanoparticle formation. It will not appear in the final solar cell device processing or eventually evaporate from large-scale manufacturing plants.

### 2.2. Microfluidic Setup and Choice of the Micromixer Chip

To conduct the experiments, we designed the microfluidic system that is illustrated in **Figure 1** and that contains two

syringe pumps, one of which is filled with the organic semiconductor solution, while the other has been prepared with the nonsolvent. In addition, a photo of the microfluidic system is shown in **Figure S1** in the Supporting Information. Tubes guide both the solvent and the nonsolvent separately into the quartz glass micromixer chip in which mixing takes place. The micromixer chip, which has to warrant best mixing of solvent and nonsolvent, is the heart of the microfluidic system. Many different micromixer chips exist to choose from with different channel widths and geometries, both of which determine the flow and the mixing of the liquids.<sup>[16]</sup> In micromixer chips, mostly frictional forces and surface tensions control the process. The mixing process is often described by the Reynolds

number  $Re = \frac{\rho \times \mu \times L}{\eta} = \frac{\mu \times L}{\nu}$ , which is the ratio of inertial

forces to frictional forces.  $Re$  depends on the density of the liquid  $\rho$ , the flow speed  $\mu$ , a characteristic linear dimension  $L$  (here: the channel width), the dynamic viscosity  $\eta$ , and the kinematic viscosity  $\nu$ .<sup>[15,17,18]</sup>

The Reynolds number is used to categorize the mixing process into two different flow regimes: laminar flow and turbulent flow. At small Reynolds numbers (typ.  $Re < 2000$ ), the flow is mostly laminar, and the liquids mix by diffusion. This leads to a rather slow mixing process. At large Reynolds numbers (typ.  $Re > 3500$ ), the inertial force is much stronger than the frictional force. The flow is mostly turbulent, and the liquids mix rather quickly. At intermediate Reynolds numbers, both laminar and turbulent elements can occur.<sup>[15,17,18]</sup> Due to the small dimensions of our microfluidic system, the Reynolds number is rather small, laminar flow prevails in straight channels and hence the mixing is rather slow.<sup>[19]</sup> To enable rapid mixing of solvent and nonsolvent, we opted for the quartz glass micromixer chip that is depicted in **Figure 2a**. It introduces vortices to the flow by implementing the split and recombine principle inside the individual mixing stages. Photos captured through an optical microscope at different stages of the mixing process are also assembled in **Figure 2**. The time stamp represents the process time elapsed since initial confluence of the P3HT:ICBA solution and the nonsolvent. The process time at each stage is estimated from the total flow rate  $Q = 3 \text{ mL min}^{-1}$  and the chip dimensions.

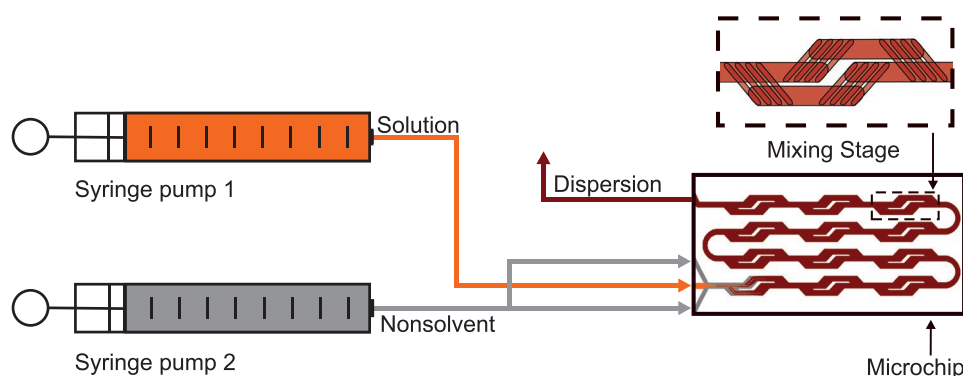


**Figure 1.** Schematic of the microfluidic system and its components. Syringe pumps feed the semiconductor solution (orange) and the nonsolvent (grey) through tubes into the micromixer chip. Differential pumping controls the mixing ratio inside the chip. The twelve mixing stages cause vortices, leading to fast mixing of solvent and nonsolvent as well as the formation of nanoparticles (red).

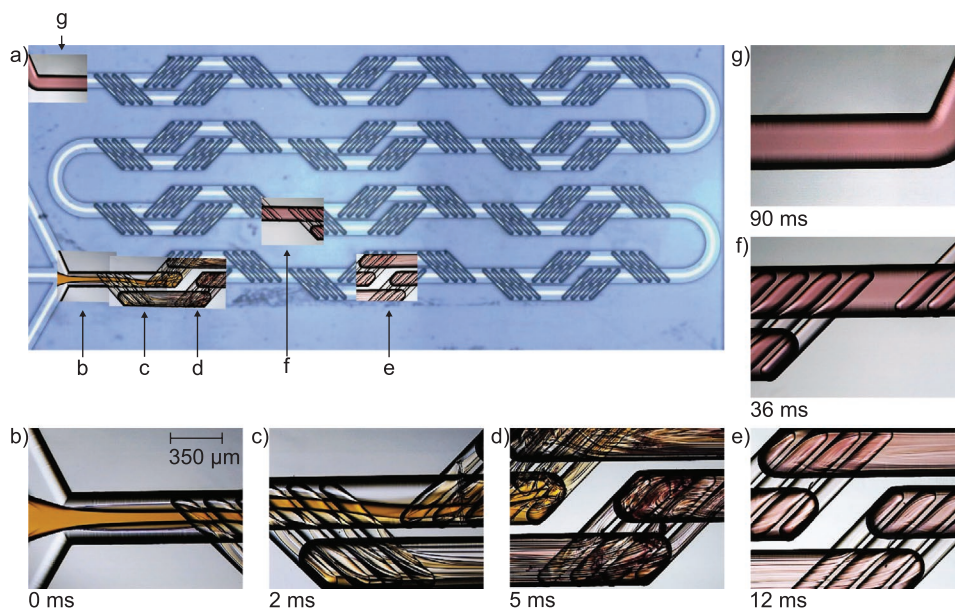


**Figure 2.** a) Tracking the solvent/nonsolvent mixture through the micromixer chip at a flow rate  $Q = 3 \text{ mL min}^{-1}$ . The time stamps represent the time elapsed since the initial confluence of semiconductor solution and nonsolvent. b) The semiconductor solution (solvent, orange) and the nonsolvent (clear) are injected right before the first mixing stage. c–e) Repeated splitting and recombination of the flow, as determined by the chip geometry, creates vortices. The color shift from orange to red indicates the aggregation of P3HT and hence the formation of nanoparticles. f) After 36 ms, the dispersion appears homogeneously colored, indicating the end of the nanoparticle formation process. g) After 90 ms, the dispersion leaves the micromixer chip.

Right after injection and initial confluence of semiconductor solution (orange, center tube) and nonsolvent (clear, top, and bottom tubes) in Figure 2b an initial laminar flow forms, followed by twelve mixing stages. Inside each mixing stage, the main channel splits into six sub-channels which shortly after recombine. Thus, vortices are created and the rapid mixing of solvent and nonsolvent is promoted. While progressing through the micromixer chip, the chloroform/ethanol mixture becomes gradually more homogenous, at the same time lowering the solubility of the semiconductor blend. Between 5 and 12 ms after the initial confluence, the color of the mixture changes from the initial orange to reddish. This change in color is the well-known bathochromic shift of P3HT, indicating its transition from a solute to an aggregated state, which is a first hint at the formation of nanoparticles.<sup>[10,20]</sup> According to the color of the dispersion, the entire mixing and nanoparticle formation process from confluence of solvent and nonsolvent to a homogeneously reddish dispersion takes about 36 ms. After 90 ms, the dispersion leaves the micromixer chip and is collected in a beaker. To finally achieve the desired dispersion concentration and to remove the chloroform, we reduced the dispersion volume by evaporation in a beaker inside a water bath.

### 2.3. Nanoparticle Formation inside the Micromixer Chip

The three primary parameters to control the fluid dynamics and to tune the nanoparticle formation are (i) the semiconductor concentration in the solvent  $c$ , (ii) the flow rate of the semiconductor solution  $Q_S$  and (iii) the flow rate of the nonsolvent  $Q_{NS}$ , the latter two of which are controlled by the pumping speeds of the syringes. Instead of  $Q_S$  and  $Q_{NS}$ , we henceforth discuss the

total flow rate through the micromixer chip  $Q = Q_S + Q_{NS}$  and the volume fraction of the nonsolvent  $\varphi_{NS} = Q_{NS} / (Q_S + Q_{NS})$  inside the microfluidic channel, which turned out to be more descriptive.

Initial tests with neat chloroform and ethanol produced a process window of  $1 \text{ mL min}^{-1} < Q < 4 \text{ mL min}^{-1}$  (at  $\varphi_{NS} > 65\%$ ). At  $Q < 1 \text{ mL min}^{-1}$ , technical limitations of the syringe pumps caused a backflow of the nonsolvent into the solvent tube, which would later lead to unwanted precipitation of the semiconductor inside the solvent tube and clogging. At  $Q > 4 \text{ mL min}^{-1}$ , the syringe pumps cannot handle the strong working loads from the flow resistance in the narrow microfluidic channel, causing the system to stop. We then investigated the process window of the nonsolvent ethanol  $\varphi_{NS}$  upon mixing with the semiconductor/chloroform solution. Here, we found a process window of  $65\% < \varphi_{NS} < 80\%$  (at an intermediate  $Q = 2 \text{ mL min}^{-1}$ ). At  $\varphi_{NS} < 50\%$ , the P3HT:ICBA blend was still soluble in the mixture of chloroform and ethanol. At  $50\% < \varphi_{NS} < 65\%$ , the chloroform fraction in the semiconductor dispersion remained too high for immediate nanoprecipitation of P3HT:ICBA, eventually leading to ripening of the nanoparticles after leaving the microfluidic channel. At  $\varphi_{NS} > 80\%$ , we again noticed a backflow of the nonsolvent into the solvent tube, which is detrimental to the process. Even though  $Q$  and  $\varphi_{NS}$  are dependent to a certain extent, both process windows have proven very reliable. Notably, the use of different pumps may widen or reduce the process windows.

Right before starting the nanoprecipitation, we preconditioned the microfluidic chip by injection of neat chloroform and ethanol with the projected flow rates. Besides cleaning of the channel, this avoided backflow of either the semiconductor solution or the nonsolvent into the respective other feed tube.

**Table 1.** Size of P3HT:ICBA nanoparticles (in nm) formed in the micro-mixer chip after injection of a P3HT:ICBA/chloroform solution with a concentration of  $c_S = 2 \text{ g L}^{-1}$  into the nonsolvent ethanol versus the total flow rate  $Q$  and the nonsolvent volume fraction  $\varphi_{NS}$ . The setup was irradiated with a spotlight LED ( $7610 \text{ W m}^{-2}$ ). The reported nanoparticle size and the standard deviation are the average of at least three different samples, each of which was measured ten times individually.

$\varphi_{NS}$ [vol%]	$Q$ [ $\text{mL min}^{-1}$ ]				
	1	1.5	2	3	4
60	$46 \pm 7.0^{\text{a}}$	$40 \pm 2.4^{\text{a}}$	$37 \pm 2.1^{\text{a}}$	$31 \pm 1.0^{\text{a}}$	$30 \pm 0.5^{\text{a}}$
66	$38 \pm 0.3$	$35 \pm 0.5$	$33 \pm 0.8$	$32 \pm 0.3$	$30 \pm 0.5$
75	$42 \pm 0.3$	$35 \pm 0.8$	$35 \pm 0.8$	$33 \pm 0.4$	$32 \pm 0.6$
80	$40 \pm 0.4$	$38 \pm 0.5$	$34 \pm 0.4$	$34 \pm 0.3$	– <sup>c)</sup>
83	– <sup>b)</sup>	$40 \pm 0.5$	$35 \pm 0.6$	$35 \pm 0.2$	– <sup>c)</sup>

<sup>a)</sup>The nonsolvent volume fraction  $\varphi_{NS}$  is too small (i.e., the solvent content is too high) leading to ripening of the nanoparticles over time; <sup>b)</sup>the low flow rate of the semiconductor solution  $Q_S$  causes backflow and uncontrolled precipitation; <sup>c)</sup>preconditioning is not possible.

By switching from neat chloroform to the semiconductor solution using a 2-way inline valve, the nanoprecipitation process was started. The dispersion was then collected at the end of the micromixer chip and immediately characterized for its nanoparticle size  $d$  (i.e., hydrodynamic diameter) in a dynamic light scattering (DLS) setup.

Initially, we chose a semiconductor concentration in solution of  $c_S = 2 \text{ g L}^{-1}$  to examine the dependence of the nanoparticle synthesis on the total flow rate  $Q$  and the volume fraction of the nonsolvent  $\varphi_{NS}$ . At  $c_S = 2 \text{ g L}^{-1}$ , varying  $Q$  between  $1 \text{ mL min}^{-1}$  and  $4 \text{ mL min}^{-1}$  as well as varying  $\varphi_{NS}$  between 60% and 83% produced nanoparticles with sizes between 30 and 46 nm as summarized in **Table 1**. We observe that, for all  $\varphi_{NS}$  and towards higher  $Q$ , the nanoparticle size decreases.

In contrast, we observed only minor influence of  $\varphi_{NS}$  on the nanoparticle size. Notably, towards either end of both process windows, the processes may not follow the general trend where high solvent content may lead to ripening of the nanoparticles over time, a low flow rate of the semiconductor solution may cause backflow and uncontrolled precipitation, or preconditioning may be impossible.

The observed smaller nanoparticle sizes for increasing flow rates  $Q$  are in accordance with an earlier report of Nikoubashman et al., who simulated the formation of polystyrene nanoparticles, where faster mixing produced smaller nanoparticles.<sup>[21]</sup>

## 2.4. Tuning the Nanoparticle Concentration and Size

For the solar cell fabrication, we seek dispersions with higher semiconductor concentration because this later reduces the number of thin-film deposition steps, which are needed to achieve the desired layer thickness. An obvious tweak to achieve dispersions with higher concentration is the increase of the P3HT:ICBA concentration in the chloroform solution. Therefore, we repeated the nanoprecipitation

**Table 2.** Sizes of P3HT:ICBA nanoparticles (in nm) synthesized in the micromixer chip after injection of a semiconductor solution with a concentration of  $c_S = 5 \text{ g L}^{-1}$  into ethanol versus the total flow rate  $Q$  and the nonsolvent volume fraction  $\varphi_{NS}$ . The setup was irradiated with a spotlight LED ( $7610 \text{ W m}^{-2}$ ). The reported nanoparticle size and the standard deviation are the average of at least three different samples, each of which was measured ten times individually.

$\varphi_{NS}$ [vol%]	$Q$ [ $\text{mL min}^{-1}$ ]		
	2	3	4
66	– <sup>a)</sup>	$49 \pm 0.5$	– <sup>a)</sup>
71	$52 \pm 1.0$	$50 \pm 0.8$	$48 \pm 0.4$
75	$54 \pm 0.6$	$51 \pm 0.5$	$50 \pm 0.6$
78	$54 \pm 0.5$	$51 \pm 0.5$	$50 \pm 0.5$
80	– <sup>a)</sup>	$55 \pm 0.5$	– <sup>b)</sup>

<sup>a)</sup>Not investigated; <sup>b)</sup>preconditioning is not possible.

experiments described in Section 2.3. with an increased initial semiconductor concentration of  $c_S = 5 \text{ g L}^{-1}$  in chloroform. This process modification did not only increase the semiconductor concentration in the dispersion, but also yielded larger nanoparticles (**Table 2**), and we observed a higher probability for clogging of the microfluidic chip.

In order to gain better control over the nanoparticle size and to enhance the colloidal stability for less clogging of the microfluidic channels, we varied the irradiation of the microfluidic chip. According to our recent experimental observations, photoexcitation of the organic semiconductors during nanoprecipitation increases the electrostatic stability of the nanoparticle dispersions.<sup>[11]</sup> In a nutshell, photoexcitation of P3HT during precipitation leads to positive charging of the nanoparticles which promotes electrostatic stabilization of the dispersion. In the blend, the residual solubility of ICBA in ethanol supports the displacement of the negative countercharges from the nanoparticles. This increased colloidal stability then leads to a smaller average nanoparticle size.

In a beaker with a path length of several centimeters, the irradiation throughout the semiconductor/solvent/nonsolvent mixture is gradually attenuated, inducing a strong variation of the process parameters within the same process and hence a strong variation of the nanoparticle size within one batch. In contrast, the microfluidic system enables the precise control of the irradiation during nanoprecipitation: due to the small channel width of  $125 \mu\text{m}$ , the absorbance is effectively homogeneous throughout the channel, and the incoming irradiation prevails throughout the volume in which the nanoparticles form. We observed that, under strong irradiation, the nanoprecipitation in the microfluidic chip produces nanoparticles with sizes down to 29 nm ( $c_S = 2 \text{ g L}^{-1}$ ). The nanoparticle sizes versus irradiance and versus concentration of the P3HT:ICBA solution are summarized in **Table 3**. The emission spectra of the light sources are provided in Figure S2 in the Supporting Information. In total darkness, i.e., upon wrapping the microchip in aluminum foil, the chip is clogged, which is likely caused by the formation of large aggregates. Some residual light ( $0.18 \text{ W m}^{-2}$ , fluorescent lamp) is already sufficient to achieve nanoparticles with sizes below 100 nm. In ambient

**Table 3.** Effect of irradiation of the micromixer chip on the P3HT:ICBA nanoparticle size ( $Q = 3 \text{ mL min}^{-1}$ ,  $\varphi_{\text{NS}} = 75\%$ ). The emission spectra of the light sources are shown in Figure S2 (Supporting Information). The reported nanoparticle size and the standard deviation are the average of at least three different samples, each of which was measured ten times individually.

Light source	Irradiance [W m <sup>-2</sup> ]	$d$ [nm]		
		at $c_S = 2 \text{ g L}^{-1}$	at $c_S = 5 \text{ g L}^{-1}$	at $c_S = 10 \text{ g L}^{-1}$
Residual light	0.18	96 ± 0.5	102 ± 0.6	127 ± 0.9
Ambient light	1.17	71 ± 0.6	84 ± 0.4	113 ± 1.9
COB-LED at 0.5 A	1440	31 ± 0.3	53 ± 2.0	95 ± 5.5
COB-LED at 1 A	2800	29 ± 0.2	47 ± 0.5	70 ± 0.9
COB-LED at 2 A	5270	30 ± 0.6	45 ± 0.2	69 ± 0.7
COB-LED at 3 A	7400	33 ± 0.4	46 ± 0.4	64 ± 0.4

light (1.17 W m<sup>-2</sup>, fluorescent lamp), the nanoparticle size decreases to 71 nm. To systematically investigate the effect of stronger irradiance, we mounted a surface-emitting chip-on-board LED (COB-LED, 2.1 cm × 2.1 cm) with a tunable operation current beneath the micromixer chip. At the maximum operation current (3 A), the electrical power of the COB-LED was 100 W. The nanoparticle size converges in the 29–33 nm regime towards stronger irradiance. At higher P3HT:ICBA concentrations in chloroform ( $c_S = 5 \text{ g L}^{-1}$ ,  $c_S = 10 \text{ g L}^{-1}$ ), larger nanoparticles form, but we again observed a reduction and convergence of the nanoparticle size towards stronger irradiation (Table 3). The reduction of the nanoparticle size under stronger irradiation results from an increase of the number of photogenerated charges, which terminate the growth of the nanoparticles at an earlier stage.<sup>[11]</sup> The convergence of the nanoparticle size towards stronger irradiation can be understood as a saturation of the number of photogenerated charges at the surface of the nanoparticle. The increase of nanoparticle size towards higher P3HT:ICBA concentrations at constant irradiation is in accordance with an earlier reports of Millstone et al. on batch-nanoprecipitated neat P3HT nanoparticles and Nikoubashman et al. on the simulation of flash nanoprecipitation of polystyrene.<sup>[21,22]</sup> Notably, the quick transition time of the solution/nonsolvent mixture through the micromixer chip of 90 ms warrants no detrimental process effects from heating under illumination.

From these investigations of the process window, a flow rate of  $Q = 3 \text{ mL min}^{-1}$  at a nonsolvent-fraction of  $\varphi_{\text{NS}} = 75\%$  appears as a good compromise to be used in all further experiments. Henceforth, a common spotlight LED with an irradiance of 7610 W m<sup>-2</sup> will provide strong irradiation.

Importantly, the implementation of a microfluidic process for the synthesis of nanoparticle dispersions produces very reproducible results. The nanoparticle size distributions in dispersions synthesized inside the micromixer chip under continuous-flow conditions and by batch nanoprecipitation in a beaker under otherwise identical conditions are compared in Figure 3. The sizes of nanoparticles synthesized in the micromixer chip are better controllable with a narrower standard deviation, which we again attribute to the increased path length of light in the beaker setup.

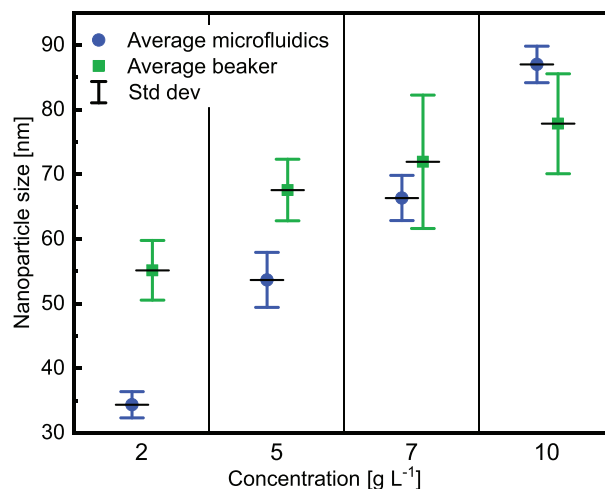


**Figure 3.** Comparison of the size of nanoparticles that were synthesized by nanoprecipitation either in a beaker (green) or in the microfluidic setup (blue) versus the semiconductor concentration in solution  $c_S$ . Each data point represents seven independent but identically conducted experiments. At all semiconductor concentrations in the initial solution, the reduced standard deviation demonstrates the superior reproducibility of the microfluidic nanoparticle synthesis. An LED spotlight was chosen as light source.

## 2.5. From Nanoprecipitation to Solar Inks

After nanoparticle formation and collection of the dispersion at the exit of the micromixer chip, the dispersion must be conditioned to be used for OSC fabrication, i.e., the chloroform must be removed and the ethanol volume must be reduced to further increase the dispersion concentration. Both, the removal of chloroform and the reduction of ethanol were achieved by thermal evaporation in a water bath (47 °C, 45 min), eventually yielding dispersions with a semiconductor concentration of  $c_D = 5 \text{ g L}^{-1}$ . For example, from 12 mL of collected nanoparticle dispersion ( $c_S = 5 \text{ g L}^{-1}$ ,  $Q = 3 \text{ mL min}^{-1}$ ,  $\varphi_{\text{NS}} = 75\%$ , irradiation with spotlight) a total of 9 mL (i.e., 3 mL of chloroform and 6 mL of ethanol) must be removed to yield a final dispersion concentration of  $c_D = 5 \text{ g L}^{-1}$  in pure ethanol. Higher dispersion concentrations  $c_D$  foster coagulation and hence long-term stable dispersions would be difficult to achieve. To collect any large aggregates from the dispersion that may have formed during this reduction step, we finally centrifuged the reduced dispersion and continued the process with the supernatant. According to the absorbance spectra in Figure S3 Supporting Information, both the semiconductor concentration and the P3HT-to-ICBA ratio prevail after centrifugation, indicating no substantial changes in the concentration and composition of the dispersion.

The resulting nanoparticle dispersions are remarkably stable. In absence of surfactants, the electrostatic stabilization of the dispersion is strong enough to prevent nanoparticle aggregation.<sup>[11]</sup> In Figure 4, the average nanoparticle size of seven individually synthesized dispersions with a concentration of  $c_D = 5 \text{ g L}^{-1}$  is shown. The nanoparticle size was measured on diluted dispersions, for which aliquots were taken from stock solutions, which were stored in a cabinet in the dark.

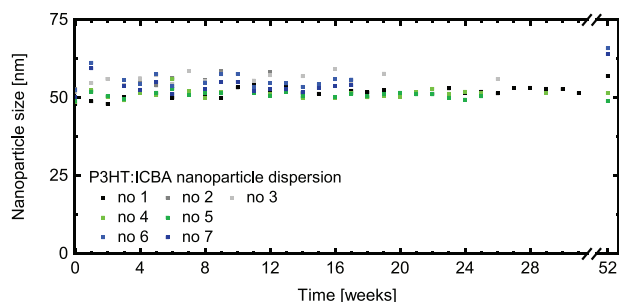


**Figure 4.** Shelf-stability of nanoparticle dispersions. The nanoparticle sizes of 7 dispersions ( $c_D = 5 \text{ g L}^{-1}$ ) synthesized by continuous-flow nanoprecipitation were monitored over one year. The size measurements were conducted by taking aliquots from stock solutions. In the second half of the experiment, only selected dispersions were measured due to small residual amounts of stock solution. None of the dispersions showed any signs of sedimentation or nanoparticle aggregation. Only two dispersions exhibited slightly increased nanoparticle sizes after one year.

Even after one year, the nanoparticle size persisted, demonstrating the excellent long-term stability of the nanoparticle dispersions that have been synthesized in the micromixer chip by nanoprecipitation.

## 2.6. Solar Cells

To investigate the suitability of the solar inks, that were synthesized by continuous-flow nanoprecipitation and subsequently reduced, for the formation of light-harvesting layers, we spin cast nanoparticulate P3HT:ICBA layers on glass substrates and examined their topography by atomic force microscopy (AFM). In **Figure 5a,b**, images of the as-cast layers from dispersions with concentrations of  $c_D = 2 \text{ g L}^{-1}$  and  $c_D = 5 \text{ g L}^{-1}$  (synthesized from semiconductor solutions with  $c_S = 2 \text{ g L}^{-1}$  and  $c_S = 5 \text{ g L}^{-1}$ , respectively) are shown (one individual deposition step). Notably, the nanoparticles within either layer appeared uniform in size and shape, and in accordance with the DLS measurements above, the nanoparticles deposited from dispersions with  $c_D = 2 \text{ g L}^{-1}$  were smaller than the nanoparticles deposited from dispersions with  $c_D = 5 \text{ g L}^{-1}$ . Still, voids are visible in both AFM images. To form closed layers, repeated deposition

by spin coating and thermal annealing to join the nanoparticles and to create an efficient BHJ are required.<sup>[10]</sup>

Next, we investigated OSCs with an inverted architecture according to the inset of **Figure 6** with photoactive layers deposited from nanoparticle dispersions ( $c_D = 5 \text{ g L}^{-1}$ ). We compared OSCs fabricated from dispersions synthesized by microfluidic continuous-flow nanoprecipitation with OSCs fabricated from dispersions synthesized by batch processing. Both nanoprecipitation processes were tailored to yield nanoparticles of similar size (microfluidics: 52 nm, batch nanoprecipitation: 58 nm). By varying the number of deposition steps, the thickness of the light-harvesting layer can be adjusted for optimum device performance. To form a smooth, closed layer, we annealed the samples after layer deposition ( $150 \text{ }^\circ\text{C}$ , 10 min). In **Table 4**, the key parameters of solar cells with nanoparticulate light-harvesting layers are summarized. The current–voltage ( $J$ – $V$ ) curves of the respective hero devices are depicted in **Figure 6**.

Four sequential deposition steps yielded nanoparticulate layers with sufficient density and a thickness  $t = 52 \text{ nm}$ . While the PCE of 4% of the corresponding OSCs lies within the common performance regime of P3HT:ICBA nanoparticulate solar cells, the performance is outstanding for 52 nm thick light-harvesting layers indicating efficient exciton dissociation and charge carrier extraction as reflected in high fill factors (FF) of up to 63%. Yet, the lower photon absorption compromises the short-circuit current density ( $J_{SC}$ ). Notably, solar cells from microfluidic nanoparticle dispersions exhibit slightly better performance than solar cells from batch-processed nanoparticle dispersions.

The key parameters of all OSCs with P3HT:ICBA layer thicknesses up to 200 nm are summarized in **Tables S1 and S2** in the Supporting Information. The performance of solar cells with thicker light-harvesting layers prepared from both batch-processed and microfluidic dispersions is shown in **Figure S4** in the Supporting Information. Towards thicker layers, the FF of the devices is reduced while the  $J_{SC}$  increases in the lower thickness regime and then decreases towards higher thicknesses, indicating higher recombination losses. Future work will aim at maintaining a high  $J_{SC}$  and higher FF in thicker devices from nanoprecipitated dispersions, while the morphology needs to be understood and optimized on the nanoscale.<sup>[9,23]</sup>

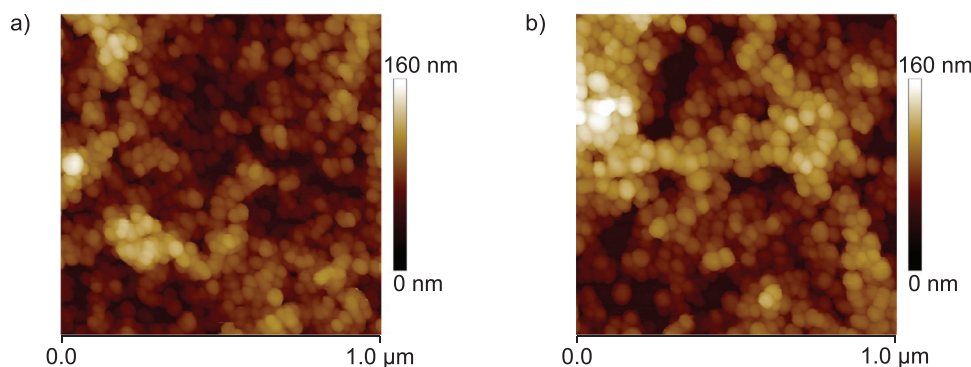


**Figure 5.** AFM topography of nanoparticulate layers deposited from dispersion (one deposition step) with a concentration of a)  $c_D = 2 \text{ g L}^{-1}$  (roughness  $R_{rms} = 19 \text{ nm}$ ) and b)  $c_D = 5 \text{ g L}^{-1}$  ( $R_{rms} = 21 \text{ nm}$ ), synthesized in the microfluidic system. At both concentrations, homogeneously distributed nanoparticles of uniform size and shape are visible.

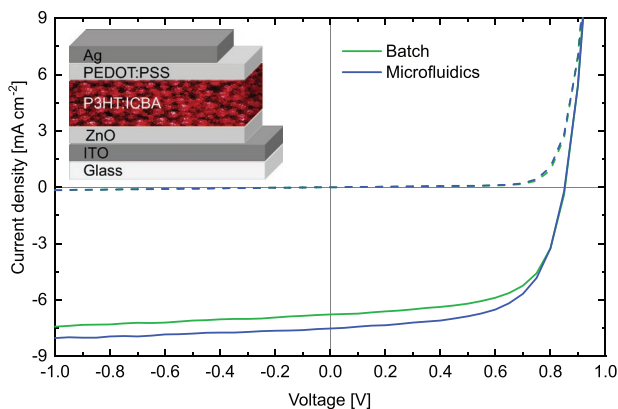


**Figure 6.**  $J$ - $V$  curves of the two “hero” nanoparticulate solar cells with photoactive layers (50 nm) deposited from dispersions that were synthesized either by batch processing or in the microfluidic system ( $c_D = 5 \text{ g L}^{-1}$ ), both showing a PCE of about 4%.

### 3. Conclusion

We have demonstrated continuous-flow nanoprecipitation in a microfluidic system for the synthesis of surfactant-free and organic bulk-heterojunction nanoparticle dispersions, which can then be used as inks for the deposition of light-harvesting layers of organic solar cells from solution. The nanoparticle size can be controlled by the semiconductor concentration, differential pumping of the semiconductor solution, and the nonsolvent as well as irradiation of the micromixer chip, producing long-term stable nanoparticle dispersions with excellent reproducibility. Using P3HT:ICBA, the respective solar cells exhibited PCEs of 4%, matching the performance of solar cells fabricated from batch-nanoprecipitated dispersions. Operating two or more microfluidic setups with different process parameters in parallel will furthermore allow the tailoring of nanoparticle size distributions in the future.

We consider the continuous-flow synthesis of organic semiconductor dispersion an important step towards the scalable production of eco-friendly inks for the large-area fabrication of organic solar cells. While in our experimental setup, the total process volume is limited by the chosen syringes, using continuous pumps and parallelizing multiple microfluidic systems will enable the reproducible large-volume synthesis of nanoparticle solar inks with continuous quality.

**Table 4.** Key parameters of the solar cells fabricated from dispersion ( $c_D = 5 \text{ g L}^{-1}$ ). The dispersions were synthesized either by continuous-flow nanoprecipitation or by batch processing in a beaker.  $t$  represents the thickness of the light-harvesting layer, #depositions represents the number of deposition steps.

Precipitation	#depositions	$t$ [nm]	$V_{OC}$ [mV]	$J_{SC}$ [mA cm <sup>-2</sup> ]	FF [%]	PCE [%]
Microfluidics	4	52	849 ± 1	7.6 ± 0.1	62 ± 1	4.0 ± 0.1
	5	65	856 ± 1	7.2 ± 0.1	61 ± 1	3.8 ± 0.1
Batch	3	53	854 ± 2	6.8 ± 0.1	63 ± 1	3.6 ± 0.1
	4	67	852 ± 1	7.0 ± 0.1	62 ± 1	3.7 ± 0.1

### 4. Experimental Section

All experiments were performed in a class 10000 cleanroom.

**Materials:** Regioregular P3HT (“4002-EE”,  $M_w = 50\text{--}70 \text{ kg mol}^{-1}$ , regioregularity > 90%) was purchased from Rieke Metals. ICBA was purchased from Solenne. All organic semiconductors were used without further purification. Analytical grade chloroform and analytical grade ethanol were purchased from Merck.

**Nanoparticle Synthesis:** P3HT and ICBA were dissolved separately in chloroform ( $c_S = 10 \text{ g L}^{-1}$ ) under stirring on a hotplate (47 °C) for at least half an hour. The blend solution was prepared by mixing the P3HT and ICBA solutions (1:1 v/v). Chloroform was added to the blend solution to yield the desired concentrations. Then the blend solution was filled in one syringe, the nonsolvent ethanol was filled in a second syringe, and both syringes were mounted onto the syringe pumps (Landgraf Laborsysteme HLL, syringe pump LA-110, High Pressure). Tubes connected the syringes and the quartz glass micromixer chip (Dolomite Microfluidics, micromixer chip, channel width: 350  $\mu\text{m}$ , channel depth: 125  $\mu\text{m}$ , branches width: 125  $\mu\text{m}$ , branches depth: 50  $\mu\text{m}$ ) as depicted in Figure 1. Unless noted otherwise, nanoparticle dispersion formed through turbulent mixing using a nonsolvent volume fraction  $\phi_{NS} = 75\%$  with  $Q = 3 \text{ mL min}^{-1}$ ,  $Q_{NS} = 2.25 \text{ mL min}^{-1}$ ,  $Q_S = 0.75 \text{ mL min}^{-1}$ , and a total volume of 4 mL, and the nanoprecipitation was performed at room temperature (20 °C) under irradiation from a spotlight LED (7610 W m<sup>-2</sup>). The raw dispersion was collected in a beaker at the exit of the micromixer chip. For reference, we conducted batch-nanoprecipitation, where P3HT:ICBA/chloroform solution (1 mL) was injected with a pipette into a beaker with nonsolvent (ethanol, 3 mL) under vigorous stirring. After nanoprecipitation, both beakers containing the raw dispersions were placed inside a water bath (47 °C) to remove the chloroform and to reduce the nonsolvent phase to yield approximately the initial semiconductor concentration ( $c_D = 5 \text{ g L}^{-1}$ ). To remove larger nanoparticle aggregates, the dispersions were centrifuged (Eppendorf, MiniSpin plus, 14 500 rpm, 2 min) and the supernatant was kept for further investigation.

**Solar Cell Fabrication:** Solar cells were built in a glovebox under nitrogen atmosphere according to the architecture depicted in the inset of Figure 6. Therefore, indium tin oxide (ITO, 135 nm) coated glass substrates were structured with hydrochloric acid following established lithography processes and then cleaned with acetone and isopropanol in an ultrasonic bath (10 min each). Afterwards, the substrates were exposed to oxygen plasma (120 s) to remove any organic residues from the ITO surface. Zinc oxide nanoparticles were synthesized following established protocols, spincoated (2000 rpm, 40 s) onto the substrates to form an electron transport layer (10 nm).<sup>[24]</sup> Then the samples were dried on a hotplate (120 °C, 10 min). Light-harvesting layers were deposited by repeated spin casting of P3HT:ICBA nanoparticle dispersion (within 90–150 s of spin coating at 1000 rpm, every 20 s an aliquot of 50  $\mu\text{L}$  of dispersion was deposited) and annealed on a hotplate afterwards (150 °C, 10 min). Poly(3,4-ethylenedioxythiophene):polystyrene sulfonate (PEDOT:PSS, HTL Solar, Heraeus) was spincoated (2000 rpm, 30 s, 25 nm) on top of the light-harvesting layer and annealed on a hotplate (120 °C, 10 min). Finally, a silver anode was thermally evaporated in vacuum (base pressure  $1 \times 10^{-6}$  mbar).

**Characterization:** The intensity-based mean size (hydrodynamic diameter) of the nanoparticle distribution in the dispersion was determined by dynamic light scattering (DLS, Zetasizer Nano ZS, Malvern Panalytical) in quartz cuvettes using standard measurement protocols. The reported nanoparticle size and the standard deviation are the average of at least three different samples, each of which was measured ten times individually. Therefore, an aliquot of the stock dispersion was separately diluted with ethanol (4  $\mu\text{L}$  dispersion with  $c_D = 5 \text{ g L}^{-1}$ , diluted in 1.2 mL ethanol, diluted concentration 0.016 g L<sup>-1</sup>, 20 °C, dynamic viscosity 1.14 mPa s, refractive index 1.361). By using only small volume fractions, the measurements of dispersions that still contain a small amount of chloroform ( $\approx 2 \text{ vol}\%$ ) are possible. The differences in nanoparticle sizes of dispersions in ethanol and the ethanol/chloroform mixtures are negligible.<sup>[11]</sup>

All layer thicknesses were measured with a Bruker Dektak XT stylus profiler.

AFM images were recorded in tapping mode on a Bruker Dimension ICON utilizing a RTESPA-300 tip.

$J$ - $V$  curves of solar cells (photoactive area 10.5 mm<sup>2</sup>) were recorded by a source measurement unit (Keithley 2420) under irradiation from a solar simulator (Xenon Sciencetech LightLine, AX-LA200, AAA, ASTM E927 AM1.5g). The solar simulator intensity was adjusted to a 1-sun-equivalent with a calibrated reference cell (Newport 91150-KG5).

## Supporting Information

Supporting Information is available from the Wiley Online Library or from the author.

## Acknowledgements

This work was financed by the Federal Ministry for Education and Research (BMBF), Germany, under contract no 03EK3571 (project TAURUS II), by KIT (Project SolarInks) and by the Helmholtz research program "Materials and Technologies for the Energy Transition (MTET)". The AFM was made available through funding by the BMBF under contract no 03EK3504 (project TAURUS). K.F. received funding from the Graduate school for Climate and Environment (GRACE). The authors acknowledge fruitful discussions with David Jones, University of Melbourne, and Holger Röhm, KIT.

Open access funding enabled and organized by Projekt DEAL.

## Conflict of Interest

The authors declare no conflict of interest.

## Data Availability Statement

The data that support the findings of this study are available from the corresponding author upon reasonable request.

## Keywords

microfluidics, organic nanoparticle dispersions, organic solar cells, surfactant-free dispersions

Received: February 24, 2022

Revised: April 21, 2022

Published online:

- [1] A. J. Moulé, *Curr. Opin. Solid State Mater. Sci.* **2010**, *14*, 123.
- [2] A. Colsmann, H. Röhm, C. Sprau, *Sol. RRL* **2020**, *4*, 2000015.
- [3] C. J. Brabec, J. A. Hauch, P. Schilinsky, C. Waldauf, *MRS Bull.* **2005**, *30*, 50.
- [4] K. Landfester, R. Montenegro, U. Scherf, R. Güntner, U. Asawapirom, S. Patil, D. Neher, T. Kietzke, *Adv. Mater.* **2002**, *14*, 651.
- [5] A. Stapleton, B. Vaughan, B. Xue, E. Sesa, K. Burke, X. Zhou, G. Bryant, O. Werzer, A. Nelson, A. D. Kilcoyne, L. Thomsen, *Sol. Energy Mater. Sol. Cells* **2012**, *102*, 114.
- [6] L. D'Olieslaeger, G. Pirotte, I. Cardinaletti, J. D'Haen, J. Manca, D. Vanderzande, W. Maes, A. Ethirajan, *Org. Electron.* **2017**, *42*, 42.
- [7] C. Xie, A. Classen, A. Späth, X. Tang, J. Min, M. Meyer, C. Zhang, N. Li, A. Osvet, R. H. Fink, C. J. Brabec, *Adv. Energy Mater.* **2018**, *8*, 1702857.
- [8] C. Xie, T. Heumüller, W. Gruber, X. Tang, A. Classen, I. Schudles, M. Bidwell, A. Späth, R. H. Fink, T. Unruh, I. McCulloch, *Nat. Commun.* **2018**, *9*, 5335.
- [9] S. Gärtner, A. J. Clulow, I. A. Howard, E. P. Gilbert, P. L. Burn, I. R. Gentle, A. Colsmann, *ACS Appl. Mater. Interfaces* **2017**, *9*, 42986.
- [10] S. Gärtner, M. Christmann, S. Sankaran, H. Röhm, E. M. Prinz, F. Penth, A. Pütz, A. E. Türel, B. Penth, B. Baumstümmler, A. Colsmann, *Adv. Mater.* **2014**, *26*, 6653.
- [11] P. Marlow, F. Manger, K. Fischer, C. Sprau, A. Colsmann, *Nanoscale* **2022**, *14*, 5569.
- [12] S. Schubert, J. T. Delaney Jr, U. S. Schubert, *Soft Matter* **2011**, *7*, 1581.
- [13] M. T. Breckenridge, T. T. Egelhoff, H. Baskaran, *Biomed. Micro-devices* **2010**, *12*, 543.
- [14] K. Hu, K. Chakrabarty, T.-Y. Ho, *Computer-Aided Design of Micro-fluidic Very Large Scale Integration (mVLSI) Biochips*, Cham, Springer, Switzerland **2017**.
- [15] G. M. Whitesides, *Nature* **2006**, *442*, 368.
- [16] Y. K. Suh, S. Kang, *Micromachines* **2010**, *1*, 82.
- [17] C. Y. Lee, C. L. Chang, Y. N. Wang, L. M. Fu, *Int. J. Mol. Sci.* **2011**, *12*, 3263.
- [18] A. Groisman, S. R. Quake, *Phys. Rev. Lett.* **2004**, *92*, 094501.
- [19] P. Tabeling, *Introduction to microfluidics*, OUP Oxford, UK **2005**.
- [20] G. Nagarjuna, M. Baghgar, J. A. Labastide, D. D. Algaier, M. D. Barnes, D. Venkataraman, *ACS Nano* **2012**, *6*, 10750.
- [21] A. Nikoubashman, V. E. Lee, C. Sosa, R. K. Prud'homme, R. D. Priestley, A. Z. Panagiotopoulos, *ACS Nano* **2016**, *10*, 1425.
- [22] J. E. Millstone, D. F. J. Kavulak, C. H. Woo, T. W. Holcombe, E. J. Westling, A. L. Briseno, M. F. Toney, J. M. J. Fréchet, *Langmuir* **2010**, *26*, 13056.
- [23] T. L. Benanti, D. Venkataraman, *Photosynth. Res.* **2006**, *87*, 73.
- [24] B. Sun, H. Sirringhaus, *Nano Lett.* **2005**, *5*, 2408.